

Evolution of Tungsten Fiber-Reinforced Tungsten-Remarks on Production and Joining

Jan Willem Coenen,* Vivian Y. S. Lee, Yiran Mao, Alasdair Morrison,
Daniel Dorow-Gerspach, Xiayue Tan, Alexis Terra, Yucheng Wu, and Christian Linsmeier

Material issues pose a significant challenge for the design of future fusion reactors. These issues require new advanced materials to be developed. W-fiber-reinforced W-composite material (W_f/W) incorporates extrinsic toughening mechanisms increasing the resistance against failure and thus granting steps toward application in a future fusion reactor. W_f/W can be produced based on chemical vapor deposition or powder metallurgical routes. In this contribution, the efforts of upscaling the production of W_f/W will be reviewed based on recent results. In addition, the activities related to enabling large-scale production for new fusion applications are being studied. Herein, two main achievements are to be highlighted. First, an upscaled production is established to produce flat tile samples for joining tests on copper and steel, and second, a new method of joining W_f/W on copper is established and tested under high heat-flux conditions.

1. Introduction of Tungsten as First Wall Material-Issues

Tungsten (W) is currently the main candidate material for the first wall of a reactor as it is resilient against erosion, has the highest melting point, shows rather benign behavior under neutron irradiation, and has low tritium retention. Extensive work has been done to qualify current materials with respect to these issues for ITER, especially for W as the first wall and divertor material,^[1] where multiple intertwined issues need to be evaluated.

Some of the main problems a future reactor is faced with are linked to the materials exposed to the fusion environment and their lifetime considerations.^[2–4] As highlighted in the study of Coenen et al.^[5]

the following interlinked issues arise: mechanical property evolution during operation, transmutation and neutron damage, ion impact, and sputtering, thermal properties (after irradiation) related to steady state heat loads and transient events, oxidation behavior during accidental air or water ingress as well as the remaining issue of fuel permeation and diffusion. Making tungsten more viable means to improve on production, upscaling, and joining of tungsten and tungsten composites. In the past, extensive work has been performed to develop new and advanced materials^[5] which has led to collaboration outside of the common fusion community to elaborate the potential of new materials for application. In this article, the efforts together with Tokamak Energy Ltd are being discussed in addition to the growing efforts of industrialization for W_f/W (Figure 1).

2. Tungsten Fiber-Reinforced Tungsten W_f/W -A Few Remarks

W_f/W or tungsten fiber-reinforced tungsten is a composite inspired by the basic of ceramics reinforcement to overcome the intrinsic brittleness and mechanical issues when using W as armor material. W_f/W utilizes tungsten wires, filaments, or yarns to achieve pseudoductility at room temperature.

Various routes are available for the production of W_f/W composites, either chemical vapor deposition (CVD)^[6,7] or powder metallurgical processes like field-assisted sintering (FAST)^[8–10] and hot isostatic pressing (HIP)^[11–15] are available. The proof


J. W. Coenen, Y. Mao, D. Dorow-Gerspach, A. Terra, Ch Linsmeier
Institut für Energie- und Klimaforschung
Forschungszentrum Jülich GmbH
52425 Jülich, Germany
E-mail: j.w.coenen@fz-juelich.de

J. W. Coenen
Department of Engineering Physics
University of Wisconsin - Madison
Madison, WI 53706, USA

V. Y. S. Lee
Tokamak Energy Ltd.
173 Brook Drive, Oxfordshire, Milton Park OX14 4SD, UK

A. Morrison
Oxford Sigma Harwell Innovation Centre
173 Curie Ave, Didcot OX11 0QG, UK

X. Tan, Y. Wu
School of Mechanical Engineering
Hefei University of Technology
Hefei 230009, China

 The ORCID identification number(s) for the author(s) of this article can be found under <https://doi.org/10.1002/adem.202300569>.

© 2023 The Authors. Advanced Engineering Materials published by Wiley-VCH GmbH. This is an open access article under the terms of the Creative Commons Attribution License, which permits use, distribution and reproduction in any medium, provided the original work is properly cited.

DOI: 10.1002/adem.202300569

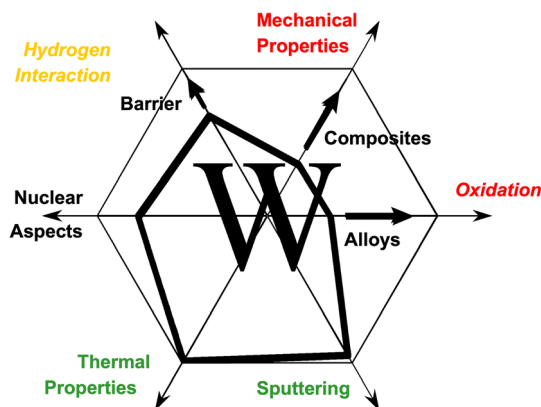


Figure 1. W as the first wall and divertor material is still facing challenges. The black lines give the status of performance with respect to ideal behavior, represented by the outline of the hexagon. The labels give the envisioned solutions and the colors the level of urgency from green to red. Nuclear aspects are discussed as part of each side and thus colored black.

of principle for CVD and PM W_f/W has been achieved and was presented in multiple publications.^[9,12,16–19]

3. Tungsten Fiber Reinforces Tungsten W_f/W -Status of Upscaling Effort

Cracking in the armor is a significant lifetime limiting factor in PFCs. Proceeding from the promising pseudoductile behavior of W_f/W shown on small-scale (40 mm) samples in 2019 year, Tokamak Energy and Forschungszentrum Juelich embarked on an 18-month project to demonstrate the upscaling of the W_f/W technology for divertor applications. This has led to both a large-scale production of short fiber W_f/W ^[20] and their study under fusion-relevant exposure conditions^[21] as well as the first successful development of powder metallurgical W_f/W .^[22] For details on the CVD W_f/W please see the study of Schwalenberg et al.^[23]

The main aim was to explore how well residual stresses scale with the component size and potentially deleterious effects on component properties in a representative divertor design. The work was in two phases involving the production, joining, and testing of (i) W_f/W disks of variant diameters between 20 and 105 mm and (ii) flat tiles of 20 mm × 50 mm in size. This work helps to elucidate the potential of using W_f/W as a plasma-facing component in a future fusion reactor. This is being driven by assessing the material properties, in particular, the ability to join W_f/W to a given cooling structure e.g., steel or copper. Here, in particular, the focus is on the stress state in the joint and the materials. Work has been performed in collaboration with Qdot.

3.1. Material Production

The work was performed on in two phases involving the production, joining, and testing of (i) W_f/W disks of variant diameters between 20 and 105 mm and (ii) flat tiles of 20 mm × 50 mm in size.

For the use in the present study, the material was produced via powder metallurgical route as described in the study of

Mao et al.^[20] Three main objectives were followed based on samples produced: upscaling, joining and characterization, and high heat-flux evaluation. Samples were produced at RWTH as well as Hefei University of Technology, with the latter focussing on the larger-scale SPS processes, using a large-scale FAST facility (LABOX-6020 Sinter Land INC).

The samples are based on the principle of porous-matrix fiber composites.^[20] First, short tungsten fibers (2.4 mm in length and 0.15 mm in diameter) were mixed with tungsten powders (5 μm average particle size), with a fiber mass fraction of 40%. Then the mixture was filled into a graphite mold with a diameter of 105 mm. Between the graphite mold and the green body, one layer of graphite foil was used between the punches and the die, to ease the sample removal after sintering, and also for sealing the gap between the punch and the die. Another layer of Mo foil was added between the sample and graphite foil to reduce carbon contamination.^[24] Afterward, the sintering was carried out at 1,400 °C for 10 min, with a heating rate of 200 °C min^{−1}. The sintering pressure was 30 MPa, which was applied when the temperature reached 800 °C. After sintering, a large disk of W_f/W with a diameter of 105 mm and a thickness of 30 mm was produced. The density of the sample was measured to be 89% using the geometric method.

Based on this, the production of test samples for joining and residual stress tests was performed. These samples are all consisting of the porous matrix material as described above and in the study of Mao et al.^[20] Four test samples were produced. Each sample is comprised of a W_f/W disk produced by FAST^[20] bonded to a 316 stainless steel disk with a 300 μm vanadium interlayer. The thickness of each disk was nominally 5 mm, resulting in a total thickness of 10 mm. Steel was used here to produce a comparable CTE mismatch as for W and Copper.

For the samples produced at RWTH Aachen (20, 40 mm) the joining to the 316L steel was performed at a temperature of 970 °C at 50 MPa for 10 min, with a heating rate of 100 °C min^{−1}, while for the samples produced at Hefei University (80 105 mm) the parameters were as followed, 850 °C 30 MPa, at a holding time of 10 min. with a heating rate of 25 °C min^{−1}. With respect to the applied cooling rate, the main difference is that cooling was controlled for the larger samples at 5 K min^{−1} whereas the smaller samples were cooled passively at about 100 K min^{−1}.

The four supplied diameters were 20, 40, 80, and 105 mm as shown in **Figure 2** and **3**.

In addition, samples were produced for testing of joining of W_f/W with copper, sizes here are 12 × 12 × 5 mm.



Figure 2. Four cylindrical stainless steel/ W_f/W test samples. From left to right: 105, 80, 40, and 20 mm.

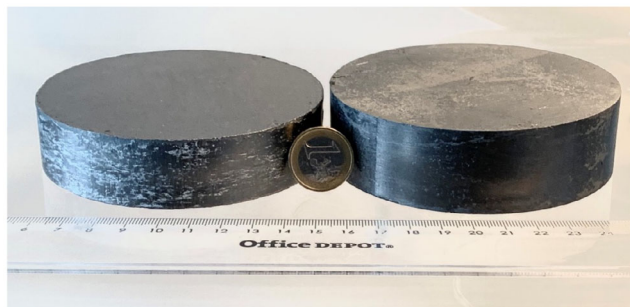


Figure 3. Large-scale PM produced W_f/W disks.

Based on the large W_f/W samples were cut to be used in actively cooled flat-tile prototypes as described in the following sections.

4. Tungsten Fiber Reinforces Tungsten-Residual Stress Tests

To assess the potential of W_f/W with respect to strength, joining, and fracture toughness, a set of tests was performed. As tungsten generally is a brittle material a joint with steel was performed to measure the residual stress in the joint and material. In addition, a quench test was performed to utilize the difference in CTE of tungsten ($4 \text{ ppm } ^\circ\text{C}^{-1}$) and steel ($16 \text{ ppm } ^\circ\text{C}^{-1}$) as a means to induce strong stresses.

4.1. Residual Stress Tests of W_f/W -Steel

Qdot Technology, on behalf of Tokamak Energy Ltd., has coordinated the characterization with respect to residual stress analysis in a set of W_f/W steel samples as described above. The cylindrical test samples were analyzed at the Advanced Forming Research Centre (AFRC)[<https://www.strath.ac.uk/research/advancedformingresearchcentre>] which conducted a series of residual stress measurements using surface and bulk residual stress measurement techniques, namely, X-ray diffraction (XRD) and the contour method, respectively.

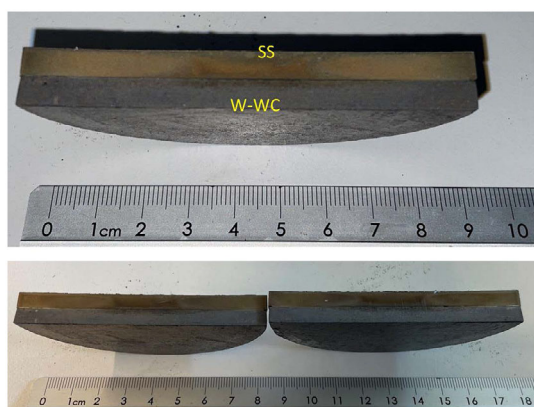


Figure 4. EDM sectioned 105 mm disk.

Each disk was halved via EDM to facilitate the planned measurements as shown for the 105 mm sample in **Figure 4**.

4.1.1. X-Ray Diffraction (XRD)

XRD determines the residual stresses in a component through the alteration of lattice plane spacing due to elastic deformation. The residual stresses in the stainless steel and tungsten-tungsten composite test samples were measured by XRD using a PROTO-LXRD diffractometer and the $\sin^2\Psi$ method. The LXRD Modular Mapping System by Proto Manufacturing Ltd. was utilized in obtaining residual stress measurements along with PROTO XRDWin 2.0 software. Measurements were obtained in accordance with the study of Fitzpatrick et al.^[25]

Trial measurements for XRD were made using the cobalt (Co) and manganese (Mn) anodes to evaluate the tungsten sides and the stainless steel sides, respectively. The W_f/W material is comprised of a matrix of pure tungsten. This was selected as the target for the XRD measurements, using the advised parameters for pure tungsten. The residual stresses within the tungsten material were calculated from the strain of $\{222\}$ plane at the Bragg reflection angle of 157° , assuming elastic Young's modulus of $E = 400 \text{ GPa}$, and Poisson's ratio of $\nu = 0.27$. For the measurements on the stainless steel side, the $\{311\}$ plane and Bragg reflection angle of 152.8° were used, assuming elastic Young's modulus of $E = 200 \text{ GPa}$ and Poisson's ratio of $\nu = 0.3$. (X-ray elastic constant: $1/2 \text{ S2 steel} : 7.18 \times 10^{-6} [1/\text{MPa}]$ W_f/W $3.2 \times 10^{-6} [1/\text{MPa}]$ X-Ray elastic constant: $-S1 \text{ steel} : 1.2 \times 10^{-6} [1/\text{MPa}]$ W_f/W $0.71 \times 10^{-6} [1/\text{MPa}]$.

The measurements were conducted at six locations per halved disk (i.e., the 20 mm disk was sectioned for the contour method (CM), then each half was measured with XRD. Measurements were performed at three locations in the stainless steel side and three locations in the W_f/W for each half, respectively. The three locations were defined as; edge (at the top edge), middle (in between the top surface and the interface), and interface. Measurements were conducted in two directions (hoop and axial) at each location making a total of 24 measurements per disk.

The XRD residual stress results for all four samples have been aggregated and are presented in **Figure 5a** (axial stress component) and **Figure 5b** (hoop stress component). For brevity, only one side of each sample is shown. Considering the axial stresses, it is clear that there is a similarity between the 20 and 40 mm samples, and the 80 and 105 mm samples. This could be expected due to their relatively comparable sizes, or due to the fact that the two smaller disks and the two larger disks were manufactured using two different methods (the specifics of the manufacturing methods lies out of the scope of this work, however, it is a potentially important observation when considering future manufacturing options). The tungsten material exhibited low axial residual stresses at the surface regardless of sample diameter.

Considering the hoop stresses from **Figure 5b**, a similar trend can be observed – however, there is an obvious increase in variation from part to part for hoop stresses compared with axial stresses. The 20 mm and 40 mm samples exhibit high hoop stresses at the top edge of the steel material (-400 MPa), however,

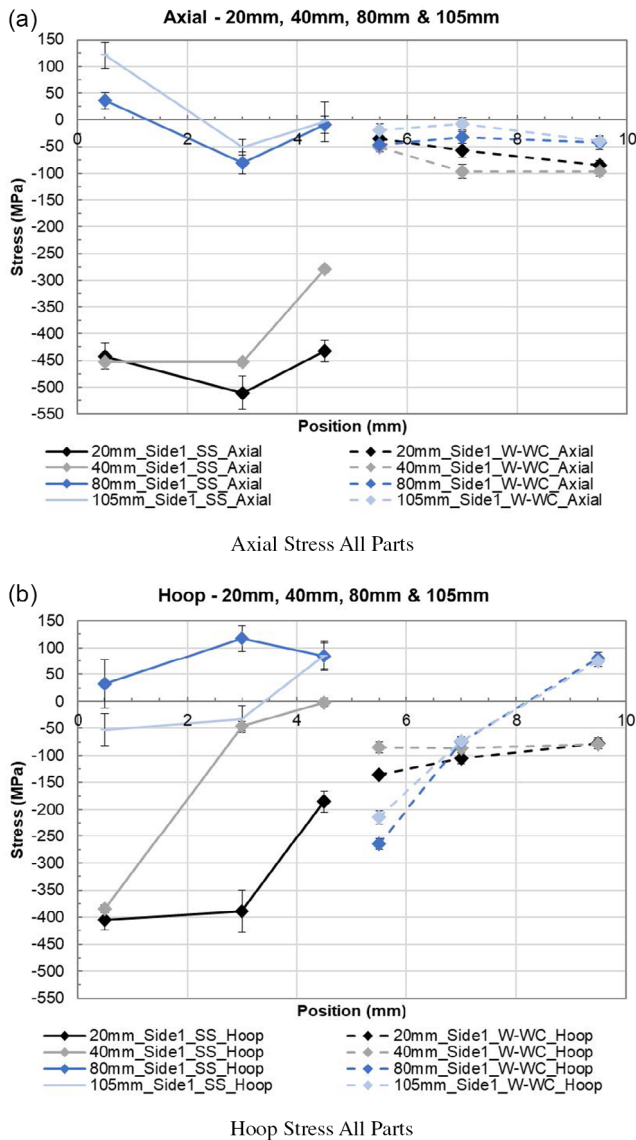


Figure 5. XRD summary a) axial stress all parts; b) Hoop stress all parts.

these decrease in magnitude close to the interface. The reduction in stress is more significant for the 40 mm compared with the 20 mm. In the tungsten material, the two larger disks show an increase in compressive hoop stresses at the interface (−220 to −260 MPa for 105 and 80 mm, respectively) compared with the smaller disks which are approximately −100 to −150 MPa.

Generally, it needs to be stated that XRD was used to validate the contour method in agreement with trends between sample sizes, but confidence in the numerical values of residual stresses is low. This is due to the 20 and 40 mm samples exhibiting fracture in the W_f/W , extending from the $W-V$ interface edge, and residual stresses exceeding yield in the steel. The primary useful output of the XRD is thus in comparing the production process of the 20/40 and 80/105 mm disks. Either the diameter or more likely cooling rates had a significant impact on component residual stresses.

4.1.2. The Contour Method (CM)

CM is a destructive method of residual stress measurement first introduced by Prime.^[26] This principle considers a cracked body subject to external loading or prescribed displacements and relates forces applied to the cracked surface to close the crack as equivalent to the stress distribution present in the body in an uncracked state, if the same geometry and experiencing the same external loading.

Figure 6 illustrates the contour method procedure. An unsectioned part (A) contains residual stresses σ_x as shown. This part is sectioned normally to the stress component of interest to result in two equal halves and a cut surface free from the out-of-plane stress component. The component is sectioned in such a way that the cracked body results in a manner as close to brittle fracture as possible, i.e., the sectioning procedure does not introduce further residual stresses due to, for example, cold work or heating. Residual stresses are released in sectioning the component and these stresses normal to the cutting plane can be obtained through considering the reverse of the cutting process and resulting deformation due to the sectioning process. The cut surface can be forced back into its original planar form through finite element simulation to obtain the original residual stress distribution. If the assumption is made that the material behaves elastically throughout the stress relief process then with reference to the stresses in Figure 6, stresses in the initial step A are equal to the sum of those in steps B and C postsectioning. As the free surface normal and shear stresses must equal zero (B), the stresses σ_x on the cut plane are equal in cases A and C and this component is obtained completely using the CM. The major advantage of this method is that it allows the measurement of a two-dimensional stress map of a component over the entire cut section. The component can be of simple or complex geometry. The CM measures type I, or macro, stresses. The CM was utilized to obtain residual stresses in each of the four disk test samples. The contour cutting axis was conducted parallel to the major axis of the discs. The measured stress component (the out-of-plane component) is therefore the hoop direction for the disks.

The 20 mm and 40 mm disks contain visibly noticeable cracks in the W_f/W material. The cracks originate close to the interface and propagate into the bulk of the W_f/W side and away from the interface. The presence of cracks is likely to influence the residual stress measurement results. During the cracking process, residual strain is released resulting in plastic deformation and crack propagation. Due to this energy release, the stresses being measured have to be considered to be different than if no cracking occurred.

The 20, 80, and 105 mm sample's CM plots are presented in Figure 7. From this image some clear trends are visible; namely, that the larger diameter parts contain extremely high axially asymmetric residual stresses. Additionally, the larger diameter parts are stress-free in the center of the part, away from the

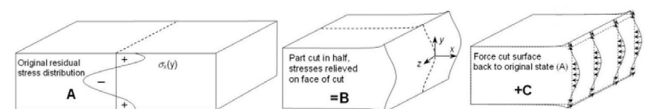


Figure 6. Principle of stress determination using the contour method.

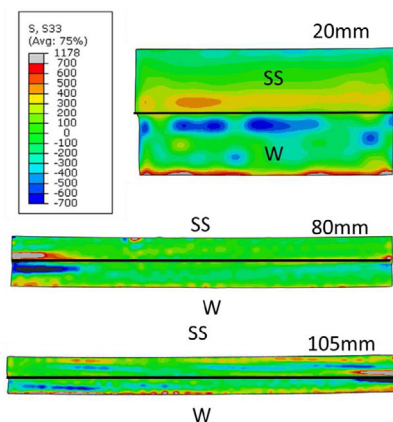


Figure 7. Summary of the contour method results (−700 To 700 MPa).

ODs, whilst the smaller 20 mm (and 40 mm) part exhibits high levels of stress in this region. This could be a significant consideration with respect to the design of the manufacturing process of real components utilizing joined SS/ W_f /W.

The XRD measurements indicated a similarity in the residual stresses found within the 20 and 40 mm parts, and the larger 80 and 105 mm parts. This pattern was continued in the contour method result analysis.

The contour method results showed that for all four parts, the tungsten side of the bimaterial sample was in compression with the stainless steel being in tension. High-magnitude stresses (reaching and exceeding the yield stress of the materials) were measured. The larger samples (80, 105 mm) were both found to contain strong asymmetry, indicating that something in the manufacturing process is causing the lack of symmetry. Also, the larger samples were both effectively stress-free in the bulk of the material. This was not the case for the smaller samples. The similarity of the stresses within the larger diameter parts (80 and 105 mm) compared with the smaller parts (20, 40 mm) indicates that either there is a strong influence from the diameter on the manufacturing-induced residual stresses, or that the manufacturing process for the larger parts was significantly different from the 20 and 40 mm parts. This is in fact due to the variation in production method as indicated above. The larger samples were, e.g., ramped much different in terms of temperature than the smaller samples.

4.2. Quench Testing

Quench tests to induce cracks (due to tensile stresses on the surface of the armor) were conducted at Warwick Manufacturing Group to study crack growth and propagation in the W_f /W composite. Samples of nominal diameters of 20, 40, and 80 mm were used for the quench tests.

The samples were prepared via powder metallurgy using a field-assisted (also described as spark plasma) sintering methodology, including for the bonding of the interlayer and bulk 316L substrate in a two-stage process (Figure 8).

In terms of surface finish, before testing, it was found that all samples have a very thin layer of graphite around the cylindrical

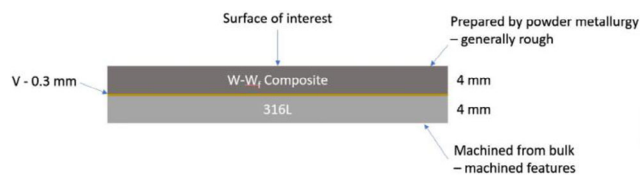


Figure 8. Sample layer materials and thicknesses.

face of the stainless steel layer. Figure 9a,b shows sections of the samples prior to testing. The antidiffusion bonding Mo foils are shown but were removed by mechanical grinding prior to testing.

Some of the samples were polished on one side after production to visually assess joint quality (see Figure 10a).

While residual stresses may have been relaxed during the notching, it was determined that the effect would be negligible in the quench test. The key factor in maximum stress on the tungsten surface (tensile in nature) is the heat transfer rate during quenching.

A Carbolite Gero vertical tube apparatus was used with a quenchant of water (with ice) directly beneath the opening of the furnace for the quenching, see Figure 11. The temperature in the core of the tube was measured using a K-type thermocouple. Samples were suspended using steel wire in the tube. The samples were heated up to 1,000 °C using flowing inert argon gas and quenched with water at 4 °C (temperature measured directly before the quench) for 30 s. Water was selected as the quenchant to induce a severe quench and induce worst-case scenario stresses at the joint interface on the at-scale sample.

When the sample reached thermal equilibrium (i.e., held at temperature for at least 20 min), the suspending wire was cut to release it under gravity into the quenchant. The sample was then recovered from the bucket after 30 s of cooling. This

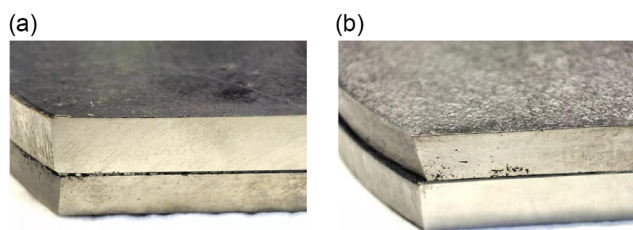


Figure 9. a) W/Wf side (upper) of 80 mm sample, b) 316L side (upper).

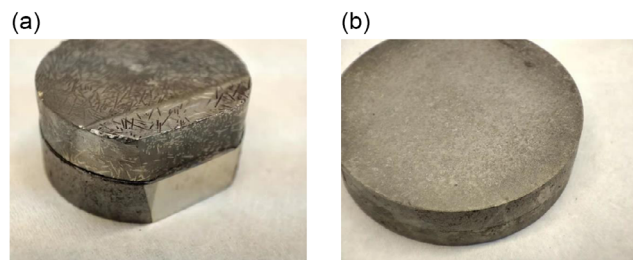


Figure 10. a) 20 mm Sample #1, notch taken prior to delivery. b) 40 mm sample.



Figure 11. Quench test set up with argon inert gas heating and water quenchant.

procedure was repeated for each sample. The temperature of the quenchant did not change throughout the tests, and the same quenchant was used for all samples.

Severe oxidation was observed on the surfaces of the samples after testing, which may be due to an insufficiently inert test atmosphere. The W side, i.e., the surface of interest, becomes yellow-green colored corresponding to WO_3 formation, hydrous- WO_3 , turns from yellow to green. The surface became flaky and when observed closely, decohesion could be seen at the fiber-matrix interface, shown in **Figure 12a**.

Nonetheless, all joints remained intact postquench even with visual observations of different shrink rates of the W_t/W and stainless-steel component. Some decohesion was observed at the fiber-matrix interface. Notably, large cracks following the fiber interface were found on the largest disk, i.e., the 80 mm diameter disk (see **Figure 12b**), which were not present on the smaller 20 and 40 mm samples.

Further analysis confirmed that some of these fractures existed on the W_t/W surface before quenching (**Figure 13a**),

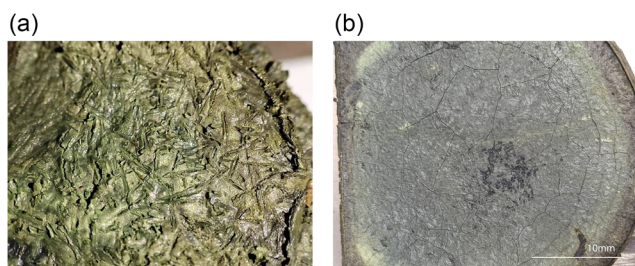


Figure 12. W_t/W composite tile surface postquench. Cracks and oxidation are evident. a) The individual fibers are 2.4 mm long, b) 80 mm sample after quenching.

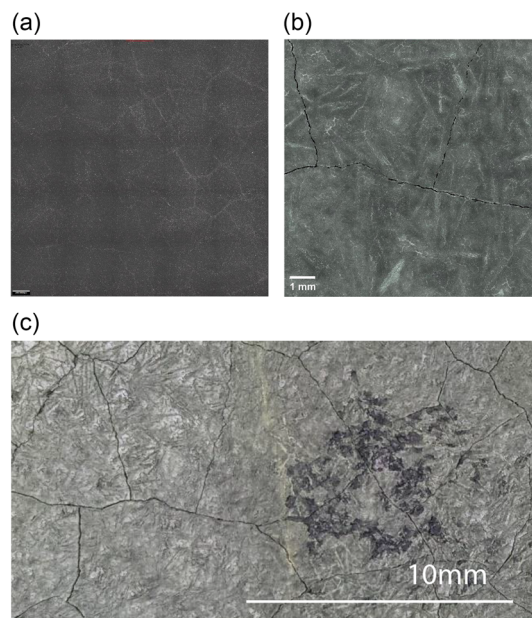


Figure 13. Optical micrograph of W_t/W surface before, a)- the individual fibers are 2.4 mm long, and after, b), quenching for the 80 mm sample - c) photograph of W_t/W surface following quenching, with evidence of fracture.

suggesting that the manufacturing process may have already generated surface cracks which were further exacerbated due to high stresses or oxidation during quenching.

Evidence of crack arrest was inconclusive from the quench study, but the reliability of the joint was promising. For information on the crack propagation in the sample, you can see a magnification of the cut in **Figure 14**.

Some cracks visible in the surface reach deep into the material being deflected partly around the visible fibers.

In **Figure 15**, a cut through the 80 mm samples is shown as a whole—clearly indicating the joint holding without damage.

It can be assumed that when cyclic quenching is applied, the cracks might traverse toward the joint.

5. Tungsten Fiber Reinforces Tungsten-Flat Tile Options

5.1. Flat-Tile Design Options

In the past multiple options for employing tungsten for fusion applications were discussed. Amongst these were flat tiles and mono-blocks.^[27,28] It was established that due to the risks associated with the joining failure of flat-tile designs, and subsequent exposure of the cooling structure to the high heat fluxes in the fusion devices mono-blocks would be the sensible choice. However, utilizing tungsten blocks facilitates the need for complex manufacturing^[29] and qualification steps. It was hence always an option to further develop the so-called flat-tile approaches for use in future devices. Among these approaches are recent developments utilizing flat tungsten armor^[30–34] similar to the ones discussed here. Critical for all of these approaches



Figure 14. Magnification of cut through 80 mm quench sample.

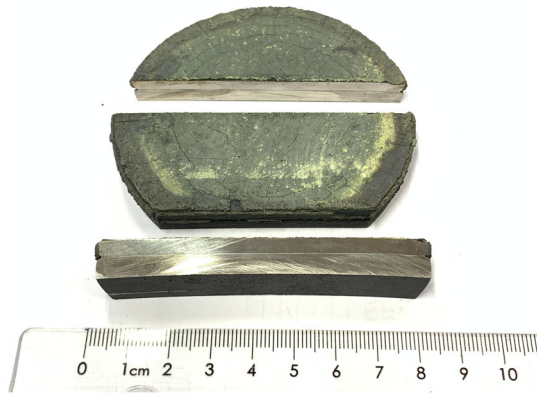


Figure 15. Cut through the 80 mm sample after quenching.

is the viability of the material choices and the joints. In the following, approaches of utilizing W_f/W joined to Cu are described.

5.2. Small Samples-Joining of W_f/W and Cu

Flat tile design requires the joint of plasma facing material (PFM) with its heat sink or structural materials. Here, porous matrix W_f/W considered as PFM is joined on copper with different joint surface treatments. The joining process is based on a liquid copper molding method. First, W_f/W was cut into a block with a dimension of $12 \times 12 \times 5 \text{ mm}^3$, then the joining surface was mechanical ground and polished to a roughness of $0.25 \mu\text{m}$.

In the following, two paths were followed - the polished surface was joined to a cooling structure or further roughened. In the case of the roughened joint surface the surface was roughened by sand blasting (here the typical scale length is the dimension of the fibers $150 \mu\text{m}$). The aim is to remove the weak porous matrix, so that the fibers can stand out forming interlocks with copper layer after the joining. Then, the joining surface was electrically polished to remove the remaining oxides on the W surface and improve the wetting. Afterward, the W_f/W block was placed in a graphite mold, and on top of it, pure copper fragments were placed. The infiltration was performed in a vacuum furnace. First, the sample was reduced in a low-pressure H atmosphere at 950°C for 12 h to remove any remaining oxides on the joining surface. Then the H flow was stopped and the temperature was then increased to $1,100\text{--}1,150^\circ\text{C}$ for 1 h to melt the Cu and realize the infiltration joining. The illustration of the process and the produced sample is shown in **Figure 16**. The cross-section of the joint is shown in **Figure 17**. It can be seen from micrographs that the joint surface is clean and dense without defects. We can even see some areas where the copper filled the voids in the porous matrix, which will consequently increase by order of magnitude the contact area between copper and tungsten.

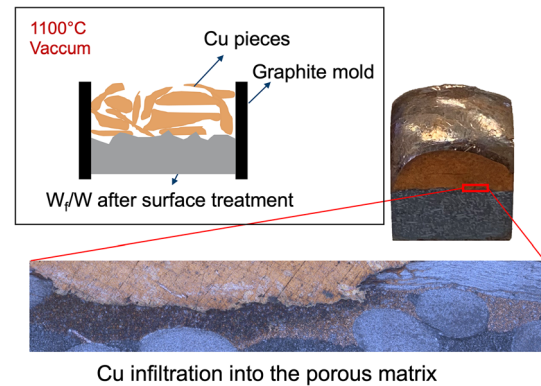


Figure 16. Joining process between Cu and porous matrix W_f/W , the diameter of the fibers visible is $150 \mu\text{m}$, the block is $12 \times 12 \text{ mm}$ in dimension.

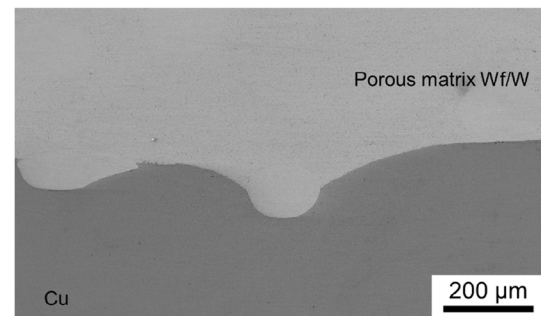


Figure 17. Microstructure of the joint between porous matrix W_f/W and Cu.

This kind of interlocking materials interface is the best way to ensure that the thermal performances will be bound by respective material thermal properties and not the interface itself. W fibers stick out forming the interlocks and improving the mechanical link between armor and heatsink. The manufacturing of the joint can be considered as successfully realized. The properties of the joint were also evaluated by a cycled high heat flux test with the electron beam JUDITH 2,^[35–37] as described in Section 6.

5.3. Joining Studies on Flat Tile Divertor Concepts

After having demonstrated the capability to produce W_f/W composites at a large scale (up to 105 mm), a disk of 105 mm diameter was produced for use as flat-tile divertor material. This phase focused on joining composite tiles onto flat-tile divertor target concepts, an example of which is shown in **Figure 18**.

The flat-tile dimensions chosen for the demonstrators in this phase were $W20 \text{ mm} \times L50 \text{ mm} \times T4 \text{ mm}$ (**Figure 19**).

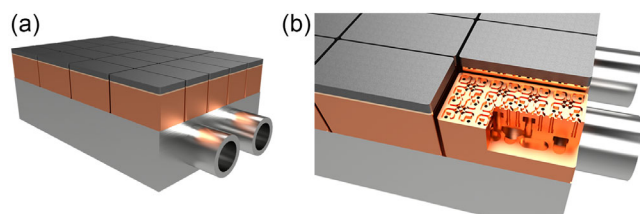


Figure 18. Sketch of one possible design for flat-tiles joint on a divertor-target cooling structure. a) Overview of a potential flattile design b) close up with potential cooling channel design (Provided by Qdot Technology Ltd, Harwell Campus, Didcot 38 OX11 0QX, UK).

The heat sink material was CuCrZr (UNS C18150) and the design was similarly based on a jet impingement gas cooling concept. Using the W_f/W composite armor, two joining methods and interlayer options were explored: (i) vacuum brazing with pure Cu interlayer and (ii) hot isostatic pressing with a functionally-graded interlayer.

5.4. W_f/W to Pure Cu Interlayer-Vacuum Brazing

A nickel-based braze filler metal was used to vacuum braze the W_f/W to a copper (C110) interlayer. Prior to the full-scale braze, wetting of the braze alloy to an off-cut of the composite tile was confirmed using a prescribed braze run for the selected filler metal.

An oversized copper interlayer (20 mm wider on either side of the tile width) was used for the full-scale braze, with a pocket matching the footprint area of the W_f/W tile to set in the braze foil. A larger thickness was accounted for grinding back to a desired flatness due to hogging after the braze run, crucial for the onward vacuum brazing stage to the CuCrZr heat sink. Conventional vacuum component cleaning by isopropanol and deionized water was applied prior to assembling the foils and tiles for brazing.

In the full-scale run, the braze alloy did not completely wet the W_f/W tile and the Cu interlayer. This was observed for 2 units in a batch of 5. It is hypothesized that the porous nature of the W_f/W tile wicked the molten alloy away from the joint and resulted in the gap shown in **Figure 20a**. This was unexpected due to the successful wetting test prior to the full-scale run. Surface preparation could have caused insufficient wetting. Another explanation is the orientation of the tile with respect to the powder metallurgy process during the production of the tile. CTE mismatch could have played a role, i.e., generating sufficient strain to disbond the tile from the Cu interlayer during the cooling phase of the braze run – however, one would then expect to observe



Visible gap between W_f/W composite tile and Cu interlayer after brazing..



Comparison of W_f/W and pure Tungsten Mock-Up

Figure 20. Mock-ups for Joining of W_f/W and pure W; a) Visible gap between $W_f=W$ composite tile and Cu interlayer after brazing; b) Comparison of $W_f=W$ and pure tungsten mock-up.

disbond across all composite tiles in the batch, which was not the case for this joining trial (**Figure 20**).

The remaining bonded tiles were processed and assembled to the heat sink structure (diffusion-bonded CuCrZr layers) for brazing. A heat treatment was prescribed as per^[38] at the end of this braze run to optimize the mechanical properties of the CuCrZr by aging, since the devices are at their solution temperature and under vacuum. Argon gas was used in the quench sequence, directed at the top of the assembly, i.e., at the top of the composite tile. The aggressive quench (almost $200\text{ }^{\circ}\text{C min}^{-1}$) in this run inevitably resulted in large thermal gradients in the bonded assembly. The diffusion-bonded heat sink layers delaminated, likely during the quench, due to weak bond strength in these layers. Here diffusion bonding is only applied on the CuCrZr heat sink structure, see the description above. Surface preparation to a tight tolerance is required for diffusion bonding and was the likely cause of the weak bond on this occasion.

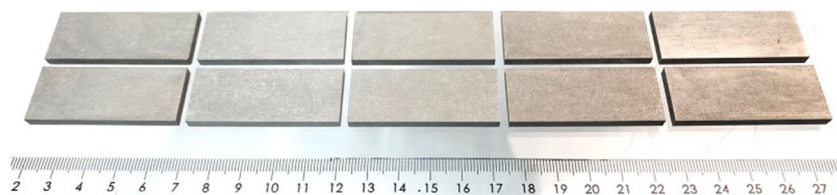


Figure 19. Sample overview - W_f/W material samples used for later joining experiments (cf. **Figure 20** the individual plates measure 4 mm in height and 20×50 mm along the respective dimensions).

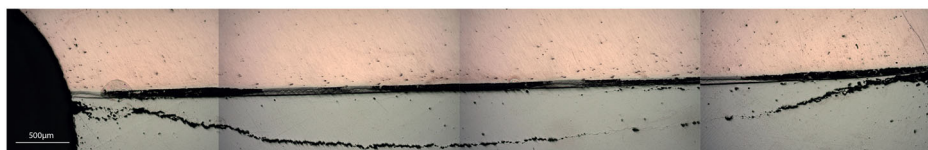


Figure 21. Crack propagating across an entire pure W tile in a W-Cu brazed joint. The pores observed are an artifact of polishing.

Visual inspection showed fractures in the delaminated armor-interlayer-heat sink (top layer) joint, with both armor variants, i.e., pure W and composite W_f/W . For the pure W, this is expected due to the intrinsic brittleness and is one of the primary modes of failure in plasma-facing components. As the fibers have been shown at a smaller scale to improve pseudo-ductile behavior, micrographs of polished joint samples were prepared to compare crack propagation in pure W and W_f/W .

In the pure tungsten tile (**Figure 21**), a clear bowed fracture line across the length of the tile is evident, extending from near the W-Cu joint to the center of the tile. The crack may have been initiated near the joint area due to higher expansion/contraction in the Cu layer. Fracture lines near the joint area are also faintly visible, and some crack branching is observed which may generate secondary fracture surfaces.

In the composite tile, cracks typically occurred along the fiber in the matrix. A longitudinal crack line can also be observed in the composite tile, as in the pure W, albeit intermittently broken up by the irregularly oriented short fibers.

Fibers around the edges of the tile can be oriented to discourage crack propagation toward the center of the tile, i.e., vertical, see **Figure 22**. The cracks can also be spotted along the tile, although it is broken up - made intermittently by the fibers. Additionally, there was a weak interface between the braze and the W_f/W tile and efforts to improve wetting should be explored if using the brazing approach. The cracks in the joint are critical at any length as they will eventually cause the joint to fail during thermal cycling. No easy way of controlling this is available which is the reason for developing mono-blocks or advanced joining see in the following section.

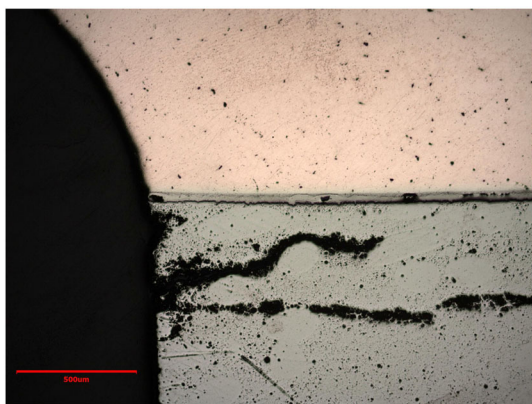


Figure 22. Crack propagating through the edge of the W_f/W sample.

6. Tungsten Fiber Reinforces Tungsten-High Heat-Flux Tests

As part of the procedure when qualifying new materials and technologies for high heat-flux components for fusion, exposures to relevant high heat-fluxes are being performed. The standard procedure includes exposure to relevant heat fluxes and evaluation of the potential for exhausting heat toward the coolant. For the base-line materials,^[35,39] this typically means exposures in one of the high heat-flux facilities.^[35,36] For W_f/W in general a few studies have already been performed wrt to its performance under high heat-flux and plasma^[20–22] where for the material itself good performance under plasma and heat-loading was established, together with high (66–80% wrt to pure) heat conductivity.

No high heat-flux tests could be performed on the samples as scribed in Section 5.3. For the material used here,^[20] the joining to the cooling structure is the main focus of the tests here. As described in Section 5.2, W_f/W is joined by roughening of the interfaces-this is then compared to standard joints and pure tungsten. Two sets of high heat-flux exposures were performed with the parameters chosen such that the copper joint is set to be at a maximum of 600 °C. This means that the heat flux chosen was at most 6 MW m^{-2} for the design of the experiment, establishing equivalence to a standard tungsten mono-block exposed to 20 MW m^{-2} where the joint is at a similar temperature. During the first series of tests up to 5 MW m^{-2} of cyclic loading (30s on/ 30s off) the joint failed early, thus the procedure for joining was adapted, and a cleaning step of the interfaces was included.

For the second set of exposures, a pure W sample $12 \times 12 \times 5 \text{ mm}$, a flat joint W_f/W on 3 mm copper, and a rough joined W_f/W on 3 mm copper were exposed where all samples were brazed to one cooling structure and exposed simultaneously (cf. **Figure 23**).

As mentioned above, the parameters were chosen to have a measure of the strength of the interface at most at 10 MW m^{-2} , based on an ANSYS simulation (**Figure 24**).

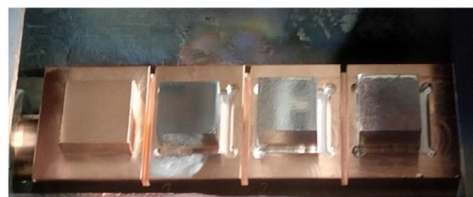


Figure 23. JUDITH 2 mock-Up for high heat-flux testing with all three types of samples ($12 \times 12 \times 5 \text{ mm}$)/joints from left to right: pure tungsten, flat joint, rough joint.

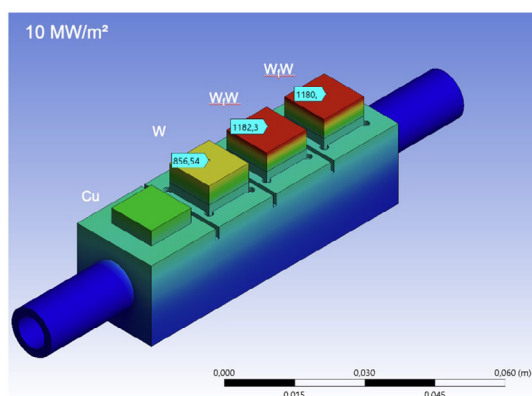


Figure 24. Temperature values from ANSYS calculation at exposure to 10 MW m^{-2} for 30 s.

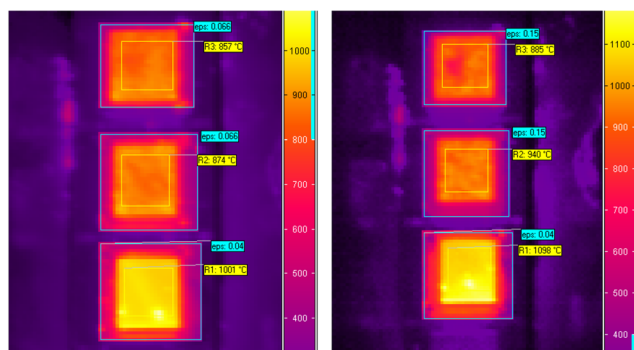


Figure 25. Thermographic images of the exposure at cycle 1 and cycle 1,000. Samples from bottom to top pure W, W_f/W flat, and W_f/W rough.

A screening was performed between 1 and 8 MW m^{-2} followed by cycling at 8 MW m^{-2} . Even after 1,000 cycles no visible change in the response to the heat-flux exposure was observed. No sign of failure was observed (cf. **Figure 25**).

The emissivity for each of the samples was determined by a parallel measurement with a pyrometer, where the only change during the series was an evolution of the emissivity on the flat W_f/W sample.

The series of cycles at 8 MW m^{-2} was followed by exposures to 10 MW m^{-2} .

In the series performed at 10 MW m^{-2} , as depicted in **Figure 26**, ejection of particles was observed and the pure tungsten samples started to overheat at one edge. The series was hence stopped at 381 cycles, also visible is an inhomogeneity of the surface temperature of the W_f/W .

After the experiment optical inspection (cf. **Figure 27**) of the material revealed that the pure W samples showed apparent recrystallization due to the high temperature, whereas both W_f/W samples showed copper droplets on the surface-the apparent reason for the cold spots on the surface in the IR images. From a side view of the mock-up, it becomes clear that the joining of the pure W samples has failed at one side, and copper has infiltrated through the porosity of both W_f/W samples, see **Figure 28**.

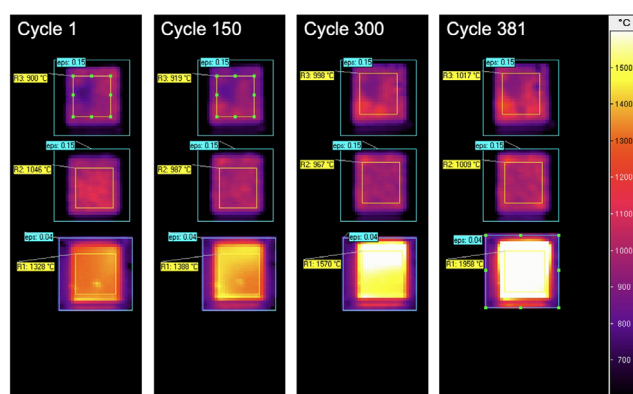


Figure 26. Thermographic images of the exposure at various cycle numbers. Samples from bottom to top pure W, W_f/W flat, W_f/W rough.

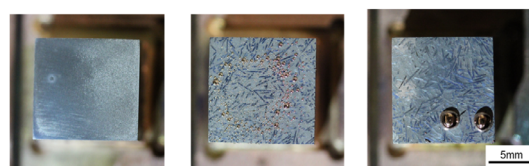


Figure 27. JUDITH 2 mock-up after exposure with all three types of samples ($12 \times 12 \times 5 \text{ mm}$)/joints - from left to right: pure tungsten, flat joint, rough joint.

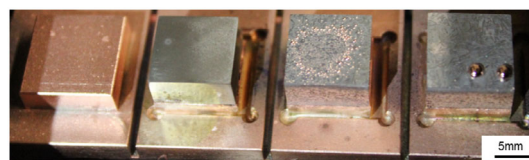


Figure 28. Sideview: JUDITH 2 mock-up after exposure with all three types of samples/joints - from left to right: pure tungsten, flat joint, rough joint.

To elucidate the behavior of Cu moving through the material the samples were sectioned and compared to pristine W_f/W Cu joint samples. In **Figure 29**, the sections are shown. EDX analysis shows that in the pristine samples, no copper can be found in the W_f/W pores, while in the exposed samples, a significant amount of copper can be measured via EDX. As the interface, the copper joint, cannot have reached a melting point the reason for this behavior needs to be further explored.



Figure 29. Samples from left to right: W_f/W -Cu rough interface before exposure, W_f/W -Cu flat interface after exposure, W_f/W -Cu rough interface after exposure - each sample is 12 mm wide.

7. Conclusion and Outlook

In this contribution, the approaches in terms of production upscaling and joining of W_f/W are reviewed. Large-scale W_f/W with 105 mm diameter and 30 mm thickness was produced using the concept of porous matrix composites, based on which, flat-tiles were manufactured. The joining of W_f/W with steel and copper was intensively performed via different methods including SPS/diffusion bonding, conventional brazing, HIP process, and copper infiltration. After joining, various characterization methods were carried out to measure the performance of the joining, including residual stress measurements, quenching tests, and high heat-flux tests. For the residual stress measurements, the XRD measurements indicated a similarity in the residual stresses found within the 20 and 40 mm parts, and the larger 80 and 105 mm parts. This pattern was continued in the contour method result analysis. The contour method results showed that for all four parts, the tungsten side of the bimaterial sample was in compression with the stainless steel being in tension. High-magnitude stresses (reaching and exceeding the yield stress of the materials) were measured.

For the high heat-flux tests, the two main statements can be seen as follows, the limit for the tests is given by the quality of the joint, and the material is easily able to handle the high heat-fluxes. In general, the mismatch of CTE can cause a failure of the joining, especially on the tungsten/ W_f/W side but the joining with W_f/W gives better behavior in terms of damage resilience. Still, the porosity of the W_f/W is one of the concerns when using it as the plasma-facing materials. In future work, the production of newly developed long fiber W_f/W with much better mechanical properties will be upscaled, together with the collaborators. Flat tiles, mono-blocks, and joining using long-fiber W_f/W will be explored.

Acknowledgements

This work has been carried out within the framework of the EUROfusion Consortium, funded by the European Union via the Euratom Research and Training Programme (grant agreement no. 101052200 - EUROfusion). Views and opinions expressed are, however, those of the author(s) only and do not necessarily reflect those of the European Union or the European Commission. Neither the European Union nor the European Commission can be held responsible for them. For this work funding was provided by the Department of Business, Energy, and Industrial Strategy, led by Tokamak Energy as part of the Advanced Modular Reactor Phase II program. The authors acknowledge the work of the Advanced Forming Research Centre (AFRC) [https://www.strath.ac.uk/research/advancedformingresearchcentre], in particular, David Easton on the Residual Stress Measurement and say thank you for the work of Qdot Technologies Ltd. [Qdot Technology Ltd, Harwell Campus, Didcot OX11 0QX, UK], e.g., Holt Wong for providing data and figures on the flat-tile designs and the quench tests.

Open Access funding enabled and organized by Projekt DEAL.

Conflict of Interest

The authors declare no conflict of interest.

Data Availability Statement

The data that support the findings of this study are available from the corresponding author upon reasonable request.

Keywords

composites, divertor, fusion, tungsten

Received: April 20, 2023

Revised: June 30, 2023

Published online: August 9, 2023

- [1] V. Philipps, *J. Nucl. Mater.* **2011**, 415, 2.
- [2] J. Coenen, S. Antusch, M. Aumann, W. Biel, J. Du, J. Engels, S. Heuer, A. Houben, T. Hoeschen, B. Jasper, F. Koch, J. Linke, A. Litnovsky, Y. Mao, R. Neu, G. Pintsuk, J. Riesch, M. Rasinski, J. Reiser, M. Rieth, A. Terra, B. Unterberg, T. Weber, T. Wegener, J.-H. You, C. Linsmeier, *Phys. Scr.* **2016**, 2016, 014002.
- [3] D. Stork, P. Agostini, J.-L. Boutard, D. Buckthorpe, E. Diegele, S. Dudarev, C. English, S. Gonzalez, A. Ibarra, Ch., G. Marbach, B. Raj, M. Rieth, M. Q. Tran, S. Zinkle, G. Federici, Technical Report EFDA(12)52/7.2, EFDA, **2012**.
- [4] R. Wenninger, M. Bernert, T. Eich, E. Fable, G. Federici, A. Kallenbach, A. Loarte, C. Lowry, D. McDonald, R. Neu, T. Puetterich, P. Schneider, B. Sieglin, G. Strohmayer, F. Reimold, M. Wischmeier, *Nucl. Fusion* **2014**, 54, 114003.
- [5] J. W. Coenen, *Adv. Eng. Mater.* **2020**, 22, 1901376.
- [6] J. Riesch, J.-Y. Buffiere, T. Hoeschen, M. di Michiel, M. Scheel, C. Linsmeier, J.-H. You, *Acta Mater.* **2013**, 61, 7060.
- [7] J. Riesch, T. Hoeschen, C. Linsmeier, S. Wurster, J.-H. You, *Phys. Scr.* **2014**, 2014 014031.
- [8] D. M. Hulbert, A. Anders, D. V. Dudina, J. Andersson, D. Jiang, C. Unuvar, U. Anselmi-Tamburini, E. J. Lavernia, A. K. Mukherjee, *J. Appl. Phys.* **2008**, 104, 033305.
- [9] B. Jasper, S. Schoenen, J. Du, T. Hoeschen, F. Koch, C. Linsmeier, R. Neu, J. Riesch, A. Terra, J. Coenen, *Nucl. Mater. Energy* **2016**, 9, 416.
- [10] Y. Mao, J. Engels, A. Houben, M. Rasinski, J. Steffens, A. Terra, C. Linsmeier, J. Coenen, *Nucl. Mater. Energy* **2017**, 10, 1.
- [11] Y. Mao, J. Coenen, J. Riesch, S. Sistla, J. Almanstötter, J. Reiser, A. Terra, C. Chen, Y. Wu, L. Raumann, T. Höschen, H. Gietl, R. Neu, C. Linsmeier, C. Broeckmann, *Nucl. Fusion* **2019**, 59, 086034.
- [12] Y. Mao, J. W. Coenen, J. Riesch, S. Sistla, J. Almanstötter, B. Jasper, A. Terra, T. Höschen, H. Gietl, M. Bram, J. Gonzalez-Julian, C. Linsmeier, C. Broeckmann, *Phys. Scr.* **2017**, T170, 014005.
- [13] Y. Mao, J. W. Coenen, J. Riesch, S. Sistla, J. Almanstötter, A. Terra, C. Chen, Y. Wu, L. Raumann, T. Höschen, H. Gietl, R. Neu, C. Broeckmann, C. Linsmeier, *Adv. Eng. Mater.* **2020**, 22, 1901242.
- [14] Y. Mao, J. W. Coenen, J. Riesch, S. Sistla, C. Chen, Y. Wu, L. Raumann, R. Neu, C. Linsmeier, C. Broeckmann, in *Spark Plasma Sintering of Materials*, Springer International Publishing, Berlin **2019**.
- [15] Y. Mao, J. W. Coenen, S. Sistla, X. Tan, J. Riesch, L. Raumann, D. Schwalenberg, T. Höschen, C. Chen, Y. Wu, C. Broeckmann, C. Linsmeier, *Phys. Scr.* **2020**, T171, 014030.
- [16] J. Coenen, Y. Mao, S. Sistla, J. Riesch, T. Hoeschen, C. Broeckmann, R. Neu, C. Linsmeier, *Nucl. Mater. Energy* **2018**, 15, 214.
- [17] H. Gietl, J. Riesch, J. Coenen, T. Höschen, C. Linsmeier, R. Neu, *Fusion Eng. Des.* **2017**, 124, 396.
- [18] J. Riesch, M. Aumann, J. Coenen, H. Gietl, G. Holzner, T. Hoeschen, P. Huber, M. Li, C. Linsmeier, R. Neu, *Nucl. Mater. Energy* **2016**, 9, 75.
- [19] J. Riesch, Y. Han, J. Almanstötter, J. Coenen, T. Höschen, B. Jasper, P. Zhao, C. Linsmeier, R. Neu, *Phys. Scr.* **2016**, T167, 014006.
- [20] Y. Mao, J. Coenen, S. Sistla, C. Liu, A. Terra, X. Tan, J. Riesch, T. Hoeschen, Y. Wu, C. Broeckmann, C. Linsmeier, *Mater. Sci. Eng. A* **2021**, 817, 141361.

- [21] Y. Mao, J. W. Coenen, A. Terra, L. Gao, A. Kreter, M. Wirtz, C. Liu, C. Chen, J. Riesch, Y. Wu, C. Broeckmann, C. Linsmeier, *Nucl. Fusion* **2022**, 62, 106029.
- [22] Y. Mao, J. W. Coenen, C. Liu, A. Terra, X. Tan, J. Riesch, T. Höschen, Y. Wu, C. Broeckmann, C. Linsmeier, *J. Nucl. Eng.* **2022**, 3, 446.
- [23] D. Schwalenberg, J. W. Coenen, J. Riesch, T. Hoeschen, Y. Mao, A. Lau, H. Gietl, L. Raumann, P. Huber, C. Linsmeier, R. Neu, *J. Nucl. Eng.* **2022**, 3, 306.
- [24] Y. Mao, C. Chen, J. Coenen, J. Riesch, S. Sistla, J. Almanstötter, A. Terra, Y. Wu, L. Raumann, T. Höschen, H. Gietl, R. Neu, C. Linsmeier, C. Broeckmann, *Fusion Eng. Des.* **2019**, 145, 18.
- [25] M. Fitzpatrick, A. Fry, P. Holdway, NPL, Great Britain, *01* **2005**.
- [26] M. B. Prime, A. T. DeWald, in *Practical Residual Stress Measurement Methods*, John Wiley & Sons, Ltd, Hoboken **2013**, p. 109.
- [27] J. Linke, *Fusion Sci. Technol.* **2008**, 53, 278.
- [28] M. Merola, G. Vieider, *J. Nucl. Mater.* **1998**, 258–263, 672.
- [29] J. Bucalossi, J. Achard, O. Agullo, T. Alarcon, L. Allegretti, H. Ancher, G. Antar, S. Antusch, V. Anzallo, C. Arnas, D. Arranger, J. Artaud, M. Aumeunier, S. Baek, X. Bai, J. Balbin, C. Balorin, T. Barbui, A. Barbuti, J. Barlerin, V. Basiuk, T. Batal, O. Baulaigue, A. Bec, M. Bécoulet, E. Benoit, E. Benard, J. Benard, N. Bertelli, E. Bertrand, et al., *Nucl. Fusion* **2022**, 62, 042007.
- [30] L. Chen, X. Liu, Y. Lian, L. Cai, *Plasma Sci. Technol.* **2015**, 17, 792.
- [31] Z. Chen, Q. Li, W. Peng, R. Wei, W. Wang, K. Jiang, J. Wang, Z. Pan, C. Xie, X. Geng, L. Huang, G. Luo, *Fusion Eng. Des.* **2021**, 172, 112919.
- [32] J. Nicholas, P. Ireland, D. Hancock, D. Robertson, *Fusion Eng. Des.* **2018**, 133, 77.
- [33] J. R. Nicholas, P. Ireland, D. Hancock, D. Robertson, *Fusion Eng. Des.* **2015**, 96–97, 136.
- [34] N. R. Schwartz, J. R. Nicholas, Z. J. Jackson, P. T. Ireland, *Phys. Scr.* **2021**, 96, 124027.
- [35] J. Linke, J. Du, T. Loewenhoff, G. Pintsuk, B. Spilker, I. Steudel, M. Wirtz, *Matter Radiat. Extremes* **2019**, 4, 056201.
- [36] C. Linsmeier, B. Unterberg, W. Coenen, R. Doerner, H. Greuner, A. Kreter, J. Linke, H. Maier, *Nucl. Fusion* **2017**, 57, 092012.
- [37] M. Roedig, E. Ishitsuka, A. Gervash, H. Kawamura, J. Linke, N. Litunovski, M. Merola, *J. Nucl. Mater.*, 307, 53, **2002**.
- [38] K. Zhang, E. Gaganidze, M. Gorley, *Fusion Eng. Des.* **2019**, 144, 148.
- [39] Y. Ueda, K. Schmid, M. Balden, W. Coenen, T. Loewenhoff, A. Ito, A. Hasegawa, C. Hardie, M. Porton, M. Gilbert, *Nucl. Fusion* **2017**, 57, 092006.